

A HYBRID PROPULSION SYSTEM FOR UAS

Dragoș Daniel ISVORANU, Petrișor-Valentin PÂRVU, Octavian GRIGORE

”Politehnica” University, Bucharest, Romania
(dragos.isvoranu@upb.ro, petrisor.parvu@upb.ro, octavian.grigore@upb.ro)

DOI: 10.19062/2247-3173.2019.21.19

Abstract: *Just like in the field of road vehicles, the tendency to increasingly electrify aeronautical systems is a topical trend triggered, first of all, by international legislation on pollutant emissions.*

The proposed subject is in line with this trend in civil aviation, investigating the use of a hybrid propulsion system (electric generator driven by a gas engine) for enhancing endurance of UAVs.

Electronically controlled ignition map for best performances of the generator is theoretically determined and then tested on an UAV testbed. Influences on the main performance features: payload and range are studied. Performances are calculated using classical civil aircraft methods (1). It is found that the better performances can be achieved with current approach.

Keywords: *Electric Aircraft, Pollution Reduction, UAV's Performance.*

1. INTRODUCTION

One of the critical requirements of UAVs in reconnaissance missions is the flight time without refueling. Duration varies considerably depending on the type of motor. Solar powered UAVs hold the long-term record (see Helios Prototype [1], the Solar Impulse 2016 project on a perpetual flight). On the other hand, this type of propulsion is recommended for those applications where the traction and payload needs are negligible.

In this study, several possibilities of UAV motorization were analyzed. For missions over 40 hours, fuel cells can be the most effective candidate for UAVs if power and payload are considerable. The same source of energy can also supply on-board electric power demand. Current technology explores the use of solid hydrogen (in the form of bars) instead of hydrogen gas in fuel cells [2]. For medium-term missions (20-40 hours), piston engines are best suited for UAV propulsion due to low fuel consumption compared to gas turbine engines of the same power [3].

It was found that for a VTOL (Vertical Take Off and Landing) UAV the best solution is a hybrid one: electric motor in quad configuration for takeoff and landing and thermal engine for fixed wing cruise flight. The main engine was fitted also with a generator to charge the batteries during cruise flight, which allows carrying smaller capacity batteries onboard.

The main engine options are either gas turbine engines (MTG) or piston engines (MP). From a theoretical point of view, the Brayton cycle at the base of the MTG operation offers an increased thermal efficiency compared to the Otto or Diesel cycle. However, with the reduction of the MTG sizes corresponding to the dimensions and load of the given UAV, a number of undesirable effects result in a reduction in the overall MTG performances [4].

With regard to MP, the two important variants to be taken into account are spark ignition engines (Otto) and compression-ignition (Diesel) engines. From a constructive point of view, both variants can be achieved in both 4-stroke and 2-stroke modes. From the point of view of thermodynamic efficiency the best results are provided by the Diesel engine due to the high compression ratio and the maximum cycle temperature close to the adiabatic flame temperature under poorly mixed conditions.

2. STATE OF THE ART

Analysis of the current state of the art is centered around correlations between power and weight as well as weight and size for various types of engine. Thus, Fig. 1 illustrates the power-to-weight relationship for piston engines, gas turbine and electric motors.

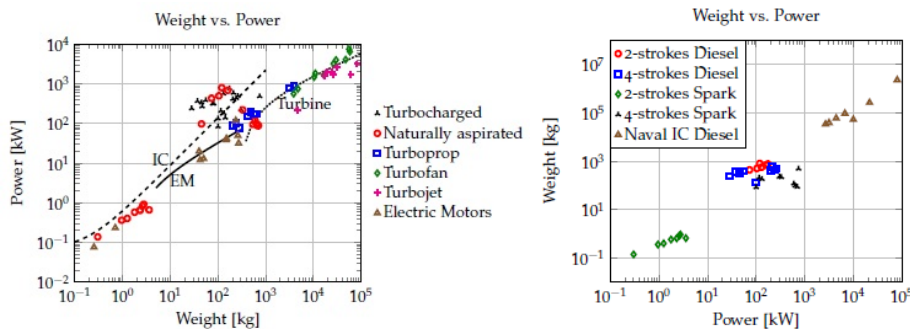


FIG. 1 Power-weight correlation for various engines. [5]

It is noted that in a logarithmic diagram, motors tend to be organized along a line, thus suggesting a $W = a + bP^c$ correlation, where W is the weight and P is the corresponding power.

For naturally aspirated piston engines, the specified correlation is especially fulfilled in the range of 0.1-30 kW and over 300 kW. In the intermediate field, there are deviations notably through the use of large bore to stroke ratio (usually > 1) as well as lightweight materials available from state-of-the-art technologies. However, these engines operate at very high speeds and are not extremely fuel efficient. At the same power, forced aspiration engines are generally heavier than those with natural aspiration due to turbocharger presence. Considering mass constraints (< 5 kg), the range of power to be investigated is between 0.2 and 10 kW. For this power range, the only options are natural aspiration and electric engines. Consequently, the analysis of forced and gas turbine engines becomes useless.

Further, for this area of power, we are interested in the ignition mode correlated with the number of engine strokes (Fig. 1).

In the field of powers of interest, we find that we are at the limit between two-stroke or 4-stroke Diesel engines and two-stroke spark ignition engines. Moreover, the field of interest is somewhat devoid of more current information. As a result of the investigation of several manufacturers, air-cooled and fuel injection engines are the most commonly used in the power range of 2.5-6 kW and with a mass below 5 kg.

The previous analysis is concretized by the representation in the following graphs.

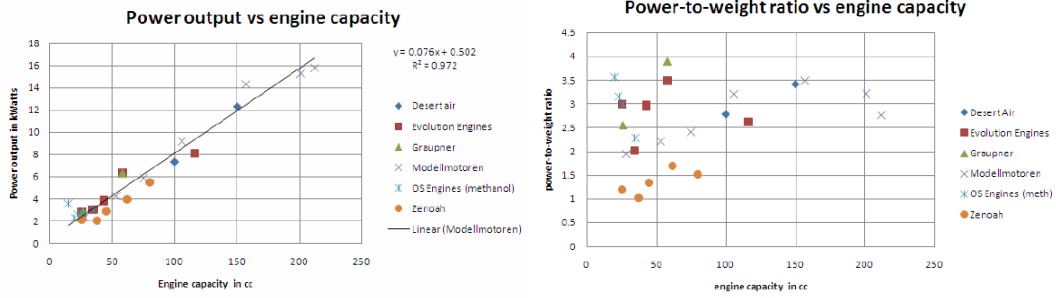


FIG. 2 Power-capacity correlation for various types of engines. [5]

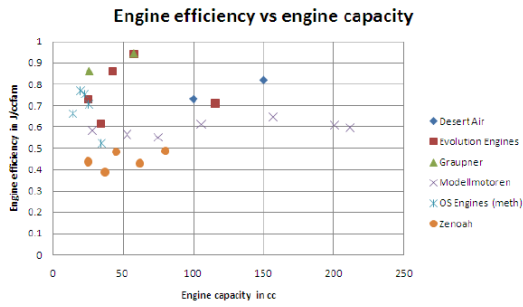


FIG. 3. The correlation between efficiency and capacity for the same engines. [5]

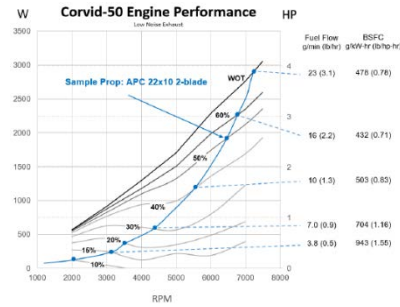


FIG. 4. Engine characteristic for corvid-50 (b50i)

The comparative analysis demonstrates, on the one hand, the linear power variation trend of 76 W/cc for the Modellmotor engines (Fig. 2). The small deviations from this trend are only characteristic of 2 and 4 cylinder variants (the last three in the upper right corner). Referring to Fig. 2, if we ignore Zenoah motors characterized by low power specific values, we conclude that for these applications the average specific power is around 2.9 kW/kg. From the last diagram (Fig. 3) results an average efficiency of 0.654 J/ccfam for the studied engines.

3. PROPULSION SYSTEM DESIGN

In view of the analysis presented in the previous paragraph, a 2-stroke, air-cooled and fuel-injected engine from the 3W-Modellmotoren 3W 55xi FI was chosen.

Unfortunately, the data provided is extremely brief and even incomplete. Thus, power, torque and specific power curves include data from both 100% and partial mode operation. Normally, for each regime it would have been necessary to specify the variation with the speed as shown in Fig. 4.

The fundamental purpose of any engine is to provide power to the shaft. Mechanical work is determined from:

$$W = \int p dV \tag{1}$$

$$W_{net_ind} = W_{brut} - W_{pomp} \tag{2}$$

Mechanical work resulting from the integration of pressure along the paths of compression and expansion is defined as crude mechanical work. Pumping work is the mechanical work associated with gas exchange processes (inlet-evacuation). The mechanical work on the shaft is obtained after the frictional mechanical work is removed from the previous expression:

$$W_{arbore} = W_{net_ind} - W_{frec} \tag{3}$$

The power generated is defined by:

$$P = \dot{W} = \int p \frac{dV}{dt} = \frac{in_r W}{60 \frac{t}{2}} \quad (4)$$

where n_r is the revolution in revolutions per minute. Torque can be determined from power in the form:

$$T = \frac{60P}{2\pi n_r} \quad (5)$$

4. THERMODYNAMIC SIMULATION OF THE ENGINE CYCLE

The development and use of simulation of the thermodynamic cycles of internal combustion engines dates from the early 1960s with the increase of the calculation capacity. At first simulations were based on various simplifications and approximations. From the point of view of burning, the most common approaches used single-zone and two-zone formulations. One of the first simulations is that of Patterson and van Wylen [7]. Simulation of the base thermodynamic cycle does not have a spatial support. However, the accuracy of the simulation can be improved if empirical relations are considered to locate the flame front. Thus, this type of model receives the quasi one-dimensional attribute.

Generally, quasi one-dimensional models are capable of accurately estimating the performance of spark-ignition engines. Given the rather high level of empirical input data, simulations can be tuned to provide a sufficiently close approximation of experimental data.

Energy conservation equations for the two-zone model are given by:

$$\frac{d(mu)_b}{d\theta} = \dot{Q}_b - p\dot{V}_b + \dot{m}_b h_b \quad (6)$$

$$\frac{d(mu)_u}{d\theta} = \dot{Q}_u - p\dot{V}_u + \dot{m}_u h_u \quad (7)$$

where the index u refers to the unburned area and the index b to the burned area. Previous equations can be developed by explaining derivatives from left members to extract derived internal energy derivatives:

$$\dot{u}_b = \frac{\dot{Q}_b - p\dot{V}_b + \dot{m}_b(h_b - u_b)}{\dot{m}_b} \quad (8)$$

$$\dot{u}_u = \frac{\dot{Q}_u - p\dot{V}_u + \dot{m}_u(h_u - u_u)}{\dot{m}_u} \quad (9)$$

Because the thermodynamic properties depend on temperature, pressure and composition, the previous derivatives can be rewritten as:

$$\dot{u}_b = \frac{\partial u_b}{\partial T_b} \dot{T}_b + \frac{\partial u_b}{\partial p} \dot{p} + \frac{\partial u_b}{\partial \phi} \dot{\phi} \quad (10)$$

where ϕ is the concentration vector of the mixture. For the unburned area the derivatives by pressure and composition are null, so that temporal temperature derivatives for the two areas can be written as:

$$\dot{T}_b = \frac{\dot{Q}_b - p\dot{V}_b + \dot{m}_b(h_b - u_b) - m_b \frac{\partial u_b}{\partial p} \dot{p} - m_b \frac{\partial u_b}{\partial \phi} \dot{\phi}}{m_b C_{v,b}} \quad (11)$$

$$\dot{T}_u = \frac{\dot{Q}_b - p\dot{V}_u + \dot{m}_u R_u T_u}{m_u C_{v,u}} \quad (12)$$

Next we need temporal derivation of the mixture pressure $pV = (m_b R_b T_b + m_u R_u T_u)$. Taking into account the constraint $\dot{m}_b = -\dot{m}_u$ deduced from the mass conservation equation results:

$$\dot{p} = \frac{\left(m_b R_b \dot{T}_b + m_b \left(\frac{\partial R_b}{\partial T_b} \dot{T}_b + \frac{\partial R_b}{\partial \phi} \dot{\phi}\right) T_b + m_b (R_b T_b - R_u T_u) + m_u R_u \dot{T}_u - p\dot{V}\right)}{v \left(1 - \frac{m_b \frac{\partial R_b}{\partial p} T_b}{V}\right)} \quad (13)$$

Continuity of volume allows us to write $\dot{V}_b = \dot{V} - \dot{V}_u$ from which it can be inferred that:

$$\dot{V}_u = \frac{(m_u R_u \dot{T}_u + \dot{m}_u R_u T_u - p\dot{V}_u)}{p} \quad (14)$$

To conclude, the five ordinary differential equations are:

$$\begin{aligned} \dot{T}_b &= \frac{\dot{Q}_b - p\dot{V}_b + \dot{m}_b (h_b - u_b) - m_b \frac{\partial u_b}{\partial p} \dot{p} - m_b \frac{\partial u_b}{\partial \phi} \dot{\phi}}{m_b C_{v,b}} \\ \dot{T}_u &= \frac{\dot{Q}_u - p\dot{V}_u + \dot{m}_u R_u T_u}{m_u C_{v,u}} \\ \dot{V}_b &= V_b \left(\frac{\dot{T}_b}{T_b} + \frac{\dot{m}_b}{m_b} + \frac{\dot{R}_b}{R_b} - \frac{\dot{p}}{p} \right) \\ \dot{V}_u &= \dot{V} - \dot{V}_b \\ \dot{p} &= \frac{\left(m_b R_b \dot{T}_b + m_b \left(\frac{\partial R_b}{\partial T_b} \dot{T}_b + \frac{\partial R_b}{\partial \phi} \dot{\phi}\right) T_b + m_b (R_b T_b - R_u T_u) + m_u R_u \dot{T}_u - p\dot{V}\right)}{v \left(1 - \frac{m_b \frac{\partial R_b}{\partial p} T_b}{V}\right)} \end{aligned} \quad (15)$$

A more complex approach takes into account the finite-speed heat transfer processes and mass losses through the segment area. In this context, it is defined by x the mass fraction that burned. The calculation procedure follows the simultaneous integration of the set of differential equations for P, T_u, T_b and subsidiary calculation of net mechanical work W , the lost heat Q_1 and thermal efficiency η .

The formulation of the first Law for the contents of the cylinder is:

$$\frac{dQ}{d\theta} - p \frac{dV}{d\theta} = \frac{dU}{d\theta} + \frac{\dot{m}_1 h_1}{\omega} = m \frac{du}{d\theta} + u \frac{dm}{d\theta} + \frac{\dot{m}_1 h_1}{\omega} \quad (16)$$

The specific volume can be written according to the burnt fraction as:

$$v = \frac{V}{m} = x v_b + (1 - x) v_u \quad (17)$$

Because $v = v(T, P)$ results:

$$\frac{dv_b}{d\theta} = \frac{dv_b}{dT_b} \frac{dT_b}{d\theta} + \frac{dv_b}{dP} \frac{dP}{d\theta} \quad (18)$$

$$\frac{dv_u}{d\theta} = \frac{dv_u}{dT_u} \frac{dT_u}{d\theta} + \frac{dv_u}{dP} \frac{dP}{d\theta} \quad (19)$$

Combining previous relationships leads to:

$$\frac{1}{m} \frac{dV}{d\theta} + \frac{VC}{m\omega} = x \frac{dv_b}{dT_b} \frac{dT_b}{d\theta} + (1-x) \frac{dv_u}{dT_u} \frac{dT_u}{d\theta} + \left[x \frac{dv_b}{dP} + (1-x) \frac{dv_u}{dP} \right] \frac{dP}{d\theta} + (v_b - v_u) \frac{dx}{d\theta} \quad (20)$$

where C is the mass loss coefficient through the area of the segments. Given that the specific internal energy of the mixture can be written as $u = U/m = xu_b + (1-x)u_u$ and $u = u(T, P)$, then:

$$\frac{du_b}{d\theta} = \left(c_{p,b} - P \frac{\partial v_b}{\partial T_b} \right) \frac{dT_b}{d\theta} - \left(T_b \frac{\partial v_b}{\partial T_b} + P \frac{\partial v_b}{\partial P} \right) \frac{dP}{d\theta} \quad (21)$$

$$\frac{du_u}{d\theta} = \left(c_{p,u} - P \frac{\partial v_u}{\partial T_u} \right) \frac{dT_u}{d\theta} - \left(T_u \frac{\partial v_u}{\partial T_u} + P \frac{\partial v_u}{\partial P} \right) \frac{dP}{d\theta} \quad (22)$$

Partial derivatives $\frac{\partial v}{\partial T}$ and $\frac{\partial v}{\partial P}$ are calculated on the basis of variable properties with temperature and pressure, depending on the composition, properties expressed in polynomial form for the various states of the mixture specified by the mass fraction x . Component $mdu/d\theta$ from the equation of first Law becomes:

$$m \frac{du}{d\theta} = mx \left(c_{p,b} - P \frac{\partial v_b}{\partial T_b} \right) \frac{dT_b}{d\theta} + m(1-x) \left(c_{p,u} - P \frac{\partial v_u}{\partial T_u} \right) \frac{dT_u}{d\theta} - \left[mx \left(T_b \frac{\partial v_b}{\partial T_b} + P \frac{\partial v_b}{\partial P} \right) + m(1-x) \left(T_u \frac{\partial v_u}{\partial T_u} + P \frac{\partial v_u}{\partial P} \right) \right] \frac{dP}{d\theta} + m(u_b - u_u) \frac{dx}{d\theta} \quad (23)$$

The term that models the decrease of mass in the cylinder can be written as:

$$\frac{dm}{d\theta} = -\frac{\dot{m}_1}{\omega} = -\frac{Cm}{\omega} \quad (24)$$

So,

$$m(\theta) = m_1 \exp[-C(\theta - \theta_1)/\omega] \quad (25)$$

represents the mass of the cylinder at a given time point from the initial mass at the beginning of the compression m_1 . The term related to the heat flow in the energy equation can be modeled in terms of heat transfer:

$$\frac{dQ}{d\theta} = -\frac{\dot{Q}_1}{\omega} = \frac{-\dot{Q}_b - \dot{Q}_u}{\omega} \quad (26)$$

$$\dot{Q}_b = hA_b(T_b - T_w); \quad \dot{Q}_u = hA_u(T_u - T_w) \quad (27)$$

in which h is the coefficient of heat transfer by convection A_u and A_b are areas of burned and non-combustion areas in contact with cylinder walls at temperature T_w . Area A_c the cylinder can be divided so:

$$A_c = \frac{\pi b^2}{2} + \frac{4V}{b}; A_b = A_c x^{1/2}; A_u = A_c(1 - x^{1/2}) \quad (28)$$

The fraction of the area in contact with the flue gas is supposed to be proportional to the fraction of the mass fraction that burned to illustrate that, because of the density difference, the flue gases occupy a larger volume than that occupied by the non-fired gases. The enthalpy of the lost mixture through the area of the segments can be calculated from the relationship:

$$h_1 = (1 - x^2)h_u + x^2h_b \quad (29)$$

The burned mass fraction can be either Wiebe's function:

$$x = 1 - \exp \left[-c \left(\frac{\theta - \theta_0}{\Delta\theta} \right)^{r+1} \right] \quad (30)$$

where θ_0 is the RAC angle of the beginning of burning, $\Delta\theta$ is the burning time and c and r are adjustable parameters, or the table function:

$$x = 0, \theta < \theta_0; x = \frac{1}{2} \left(1 - \cos \left(\frac{x(\theta - \theta_0)}{\Delta\theta} \right) \right); x = 1, \theta > \theta_0 + \Delta\theta \quad (31)$$

Considering unbound gas as an open chemical reagent that loses mass, it can be shown that:

$$-\dot{Q}_u = \omega m (1 - x) T_u \frac{ds_u}{d\theta} \quad (32)$$

Since $s_u = s_u(T_u, P)$, results

$$c_{p,u} \frac{dT_u}{d\theta} - T_u \frac{dv_u}{dT_u} \frac{dP}{d\theta} = \frac{-h_{A_u}}{\omega m (1-x)} (T_u - T_w) \quad (33)$$

Taking into account all the equations mentioned so far, the following variables can be defined:

$$\begin{aligned} A &= \frac{1}{m} \left(\frac{dV}{d\theta} + \frac{VC}{\omega} \right) \\ B &= \frac{h_{A_c}}{\omega m} \left[\frac{1}{c_{p,b}} x^{1/2} (T_b - T_w) \frac{\partial v_b}{\partial T_b} + \frac{1}{c_{p,b}} (1 - x^{1/2}) (T_u - T_w) \right] \\ C &= -(v_b - v_u) \frac{dx}{d\theta} - \frac{\partial v_b}{\partial T_b} \frac{h_u - h_b}{c_{p,b}} \left[\frac{dx}{d\theta} - \frac{(x - x^2)C}{\omega} \right] \\ D &= x \left[\frac{T_b}{c_{p,b}} \left(\frac{\partial v_b}{\partial T_b} \right)^2 + \frac{\partial v_b}{\partial P} \right] \\ E &= (1 - x) \left[\frac{T_u}{c_{p,u}} \left(\frac{\partial v_u}{\partial T_u} \right)^2 + \frac{\partial v_u}{\partial P} \right] \end{aligned} \quad (34)$$

The equations to be integrated are:

$$\begin{aligned} \frac{dP}{d\theta} &= \frac{A+B+C}{D+E} \\ \frac{dT_b}{d\theta} &= \frac{-h_{A_c}(T_b - T_w)}{\omega m c_{p,b} x^{1/2}} + \frac{T_b}{c_{p,b}} \frac{\partial v_b}{\partial T_b} \frac{A+B+C}{D+E} + \frac{h_u - h_b}{x c_{p,b}} \left[\frac{dx}{d\theta} - \frac{(x - x^2)C}{\omega} \right] \\ \frac{dT_u}{d\theta} &= \frac{-h_{A_c}(1 - x^{1/2})(T_b - T_w)}{\omega m c_{p,b}(1 - x)} + \frac{T_u}{c_{p,u}} \frac{\partial v_u}{\partial T_u} \frac{A+B+C}{D+E} \end{aligned} \quad (35)$$

$$\frac{dW}{d\theta} = P \frac{dV}{d\theta}$$

$$\frac{dQ_1}{d\theta} = \frac{hA_c}{\omega} [x^{1/2}(T_b - T_w) + (1 - x^{1/2})(T_u - T_w)]$$

$$\frac{dH_1}{d\theta} = \frac{Cm}{\omega} [(1 - x^2)h_u + x^2h_b]$$

The above equations are numerically integrated in Matlab. Input data are bore, stroke, speed, compression ratio, mass loss coefficient, heat transfer coefficient, cylinder temperature, initial pressure and temperature. The initial temperature for the burnt area is estimated from the calculation of the adiabatic temperature of the flame based on the enthalpy at the moment of initiation of the spark. If $x < 0.001$, the system is considered to be composed only of non-fired gases and if $x > 0.999$, we only deal with flue gases. The program contains a routine for the expression of the thermodynamic properties depending on the residual fraction (flue gas from the previous cycle) and another routine for calculating the composition and the equilibrium properties for a chemical reactive mixture.

As the compression ratio is completely unknown, we had to try several sets of values for the input data and compare the power obtained with the manufacturer's data. For this, it is necessary to estimate the power lost by friction and pumping (2), (3). The power lost through friction inside the cylinder depends on the cylinder and the speed can be estimated from the relationship:

$$P_f = (100000 + 20n_r)V_s n_r / 60 \tag{36}$$

The power lost due to the pumping process depends to a large extent on the inlet pressure P_1 and the exhaust pressure in the environment P_e

$$P_p = (P_e - P_1)V_s n_r / 60 \tag{37}$$

With this data the following results were obtained:

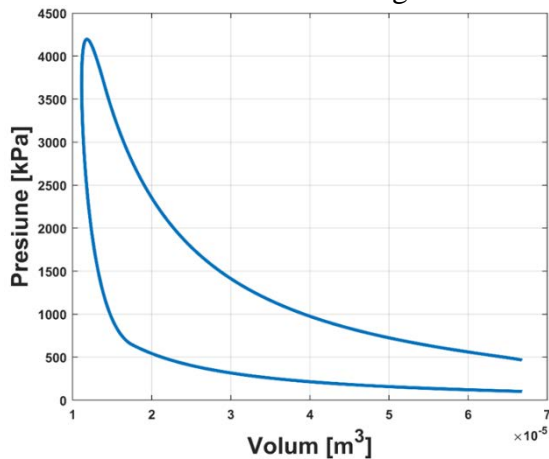


FIG. 5 Variation of cylinder pressure for no mass exchange evolutions.

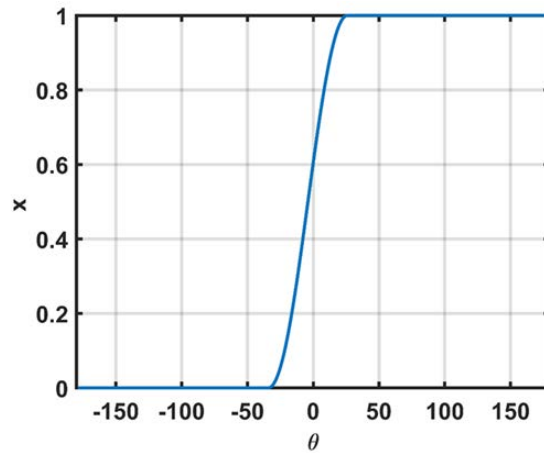


FIG. 6 The variation of the burning mass fraction burned with the crankshaft angle.

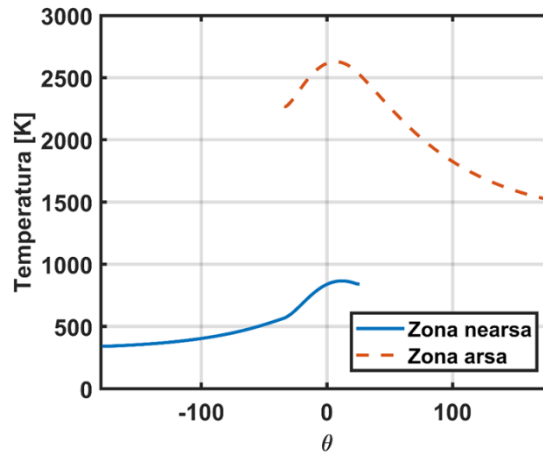


FIG. 7. Temperature variation in the burned and unburned area with the crank angle.

Since the engine test was carried out with the attached generator, the power to the shaft must be penalized by taking into account the power absorbed by the generator. The variation of this generator power is specified in Fig. 8. The results of the simulation are compared with the experimental results in Fig. 9.

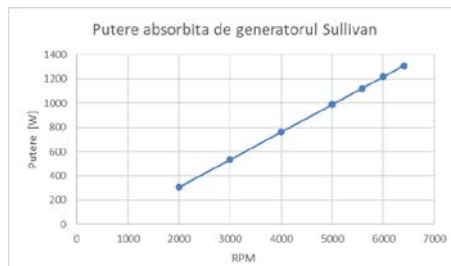


FIG. 8 Power absorbed by the generator.

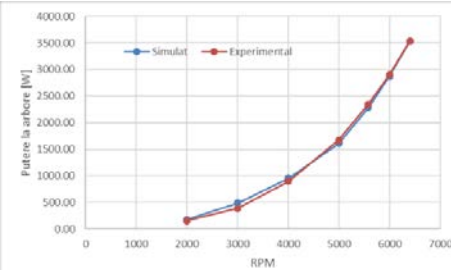


FIG. 9 Simulation comparison and SLS experiment for engine 3w 55xi fi.

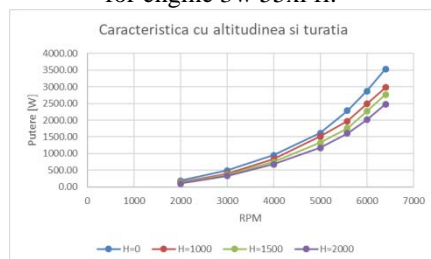


FIG. 10 Characteristics with turning and altitude.

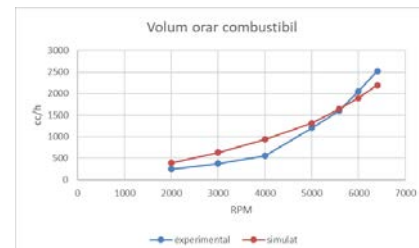


FIG. 11 Comparison of fuel consumption between simulation and SLS experiment for the engine 3w 55xi fi.

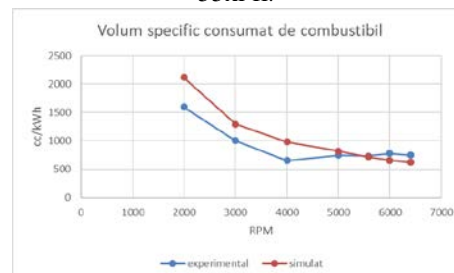


FIG. 12 Specific fuel consumption comparison between simulation and SLS experiment for the engine 3w 55xi fi.

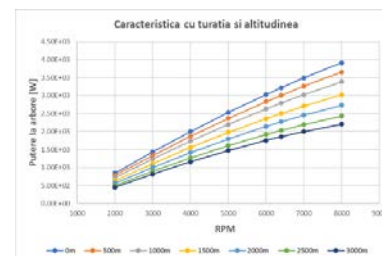


FIG. 13 Shaft power.

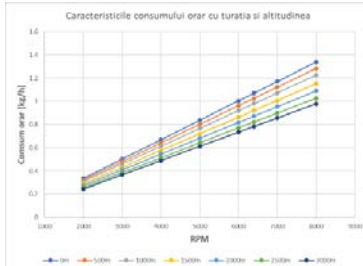


FIG. 14 Hourly consumption

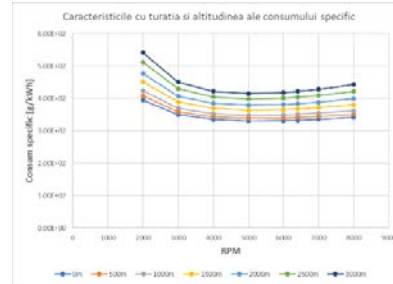


FIG. 15 Specific consumption

The results are quite promising, especially in terms of sea level power variation. Hourly and specific consumption are somewhat affected by less accurate engine yield estimation, so errors that fall within the 10% margin of uncertainty about data used in the simulation.

5. PERFORMANCES OF THE HYBRID PROPULSION FIXED WING VTOL UAV

The geometric reference data taken into account for the performance calculations are shown in Fig. 16, considering a reference origin at the nose of the fuselage, the O_x axis along the fuselage, the O_y axis along the wing span, and the O_z axis perpendicular to the Oxy plane pointing downwards.

The mass of the structural components was estimated by statistical methods and their weight centers were determined by considering the average density introduced in the 3D CAD model shown in Fig. 17.

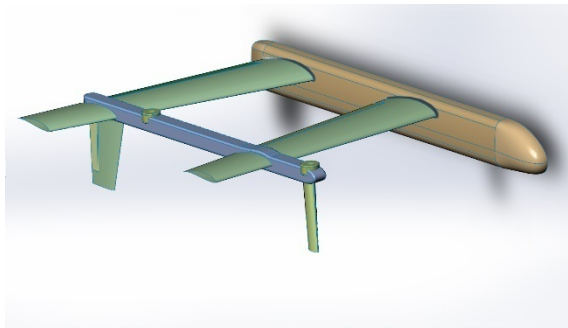


FIG. 16 Reference geometry

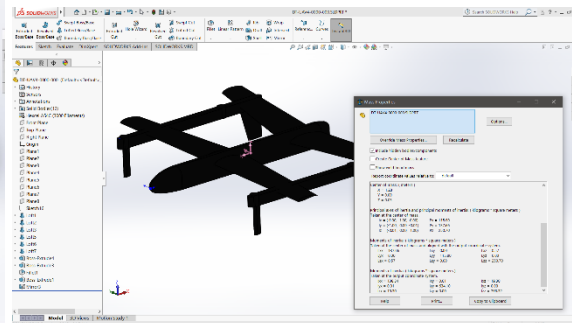


FIG. 17 Aircraft balance

The aerodynamic characteristics of the aircraft were determined by a method developed by the authors, based on the work [8]. The results were compared with those obtained from specialized software systems:

- XFLR5, [9], which uses the Vortex Lattice Method for small Re numbers;
- AVL, [10], a program for aerodynamics and flight dynamics analysis of rigid aircraft of arbitrary configuration. It uses a model of Extended Vortex Lattice for lifting surfaces, along with a thin body model for fuselage and nacelles. General nonlinear flight states can be specified. Dynamic Flight Analysis combines a complete aerodynamic alignment for any flight state with the specified mass properties;
- Advanced Aircraft Analysis, [11], produced by DARcorporation, is a comprehensive airplane design program that gives users full authority over the entire preliminary design process. From weight and performance to aerodynamic analysis and stability and control, all aspects of design at every step of the road can be monitored.

- RDSwin allows engineers to take up an aircraft project from the first conceptual point of view through functional analysis, resulting in performance, endurance, weight and cost. RDSwin integrates design (CAD), aerodynamic calculation, mass estimate, propulsion, stability and control, sizing, performance and cost analysis.

Most performance calculations and flight dynamics have gone from defining a basic, stationary movement, usually straight cruise flight uniform. The aerodynamic characteristics of the airplane will be equilibrium. Therefore, the equilibrium polar determined by calculation or experiment is used.

Starting from the expression of the moment of pitch according to the flight incidence and the elevator deflection, we can determine for each angle of attack the equilibrium by solving the equation:

$$C_m(\alpha, \delta_e) = 0 \tag{38}$$

6. PROPELLER DESIGN, AVAILABLE POWER

The next step to determine the performance in uniform motion of the aircraft requires the determination of available power depending on speed and fuel consumption; it is necessary to obtain:

- Power supplied by the engine to the propeller shaft (Fig. 13)
- Propeller characteristics: coefficients of traction C_T , moment of drag C_Q , used power C_P and propeller efficiency η (Fig. 18)
- Specific fuel consumption (Fig. 15)

Calculation of the propeller characteristics was done with the propCalc program [12]. The calculated propeller geometry is given in Fig. 18 and its features are shown in Fig. 19.



FIG. 18 Geometry of the propeller

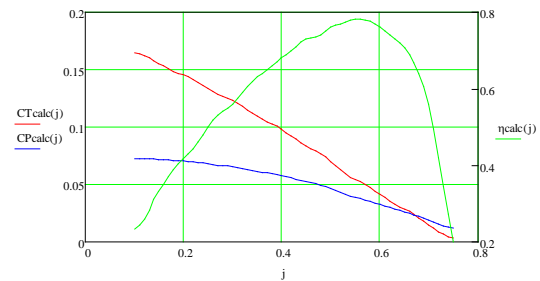


FIG. 19 Propeller features

The algorithm for determining the power available by the speed implies the determination of the propeller speed from the balance between the power consumed by the propeller and the power supplied to the shaft.

At a given altitude the $P_a(\Omega)$ function is extracted (Ω = propeller speed in rad/s), then, from the propeller characteristics, the power consumed by the propeller is calculated with:

$$J = \frac{60V}{\Omega D_{prop}}; P_e(\Omega, V) = \rho(H) \left(\frac{\Omega}{60}\right)^3 D_{prop}^4 C_{P_{calc}}(J) \tag{39}$$

where $D_{prop} = 21'' = 0.533m$ is propeller diameter, and $P_{prop} = 11'' = 0.279m$ is propeller pitch.

The steady speed is found by solving the equation below for a selected flight speed:

$$P_e(\Omega, V) - P_a(\Omega) = 0 \rightarrow \Omega(V) \tag{40}$$

Finally, the available power is given by (Fig. 20):

$$P_d(V) = \eta(J(\Omega(v), V))P_e(\Omega(V), V) \quad (41)$$

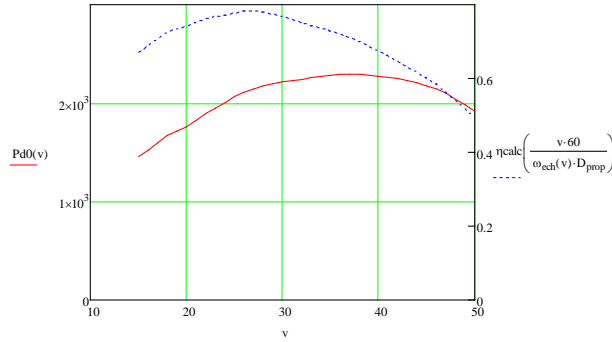


FIG. 20 Available power

7. FLIGHT PERFORMANCES IN SIMETRIC MOVEMENTS IN THE VERTICAL PLANE, FLIGHT ENVELOPE

The limits of the rectilinear flight velocity are determined at each altitude of calculation by the intersection of available and necessary power for maximum speed and by determining the speed corresponding to the minimum required power. The minimum required power is determined with the relations:

$$C_L = \frac{2Wg}{\rho(H)SV^2}; \quad P_n(V) = 0.5\rho(H)SV^3C_D(C_L) \quad (42)$$

and the intersection $P_d = P_n$ gives us the speed of balance $V2$. The minimum power point allows us to find the minimum speed $V1$:

$$V2_0 = \text{root}(P_n(V) - Pd_0(V), V) = 43.41 \text{ m/s}$$

$$V1_0 = \text{root}\left(\frac{d}{dV}P_n(V), V\right) = 19.94 \text{ m/s} \quad (43)$$

This algorithm was shown graphically in Fig. 21, where the equilibrium flight incident was also represented at each speed. Note that the steady-state incidence is negative $\alpha_{ech} = -1.4$ deg., but it has a small value, so it is acceptable.

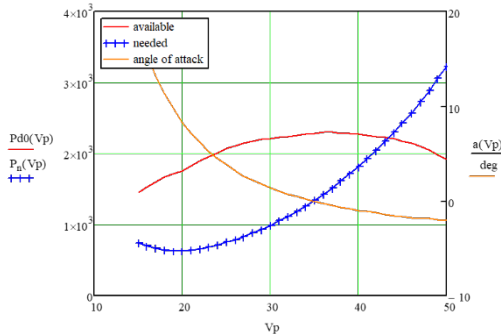


FIG. 21 Method of power available and required (H = 0m)

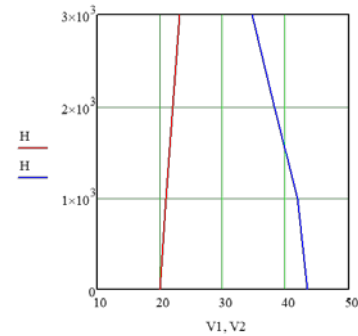


FIG. 22 Flight envelope

Doing the same for all altitudes for which the outputs for the shaft power supplied by the engine are calculated: 1000, 2000 and 3000m, it can be obtained $V2(H)$ and $V1(H)$, which are graphically represented in the flight envelope of Fig. 22.

For the study of the uniform rectilinear climb, also the necessary and available power method is applied starting from the stationary motion equations:

$$C_L = \frac{2Wg \cos(\gamma)}{\rho(H)SV^2}; \quad P_n(V) = 0.5\rho(H)SV^3C_D(C_L) + Wg * \sin(\gamma) \quad (44)$$

where through γ the trajectory slope was noted. For a given altitude and a flight slope we determine the necessary C_L as a function of velocity. From the equilibrium polar is determined C_D and the $P_n(V)$.

Intersect the required power with the available power and determine the speed. The pairs (γ, V) such obtained are used to plot the climbing characteristic (Fig. 23), in coordinates $(V\cos(\gamma), V\sin(\gamma))$.

Based on the climbing characteristic, it can be concluded that:

- The maximum ascending speed, in steady state, is 3.8m/s, at a flight speed of 25.9m/s, and
- The maximum climb slope is 9deg. At a flight speed of 22.6m/s

Gliding flight is treated similarly, with the difference that we have no available power and the slope is negative. The gliding flight characteristic is shown in Fig. 24.

The conclusion of the gliding flight study is that:

- The minimum descent speed in stationary mode is 2m/s at a flight speed of 23m/s due to limitation given by the maximum speed, and
- The minimum gliding slope is 5 degrees, at a flight speed of 21m/s

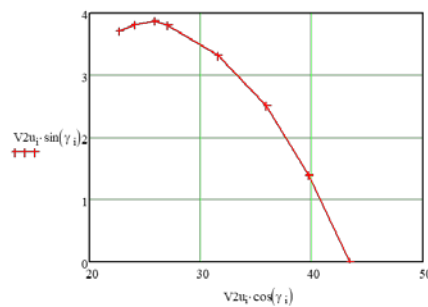


FIG. 23 The climbing characteristic

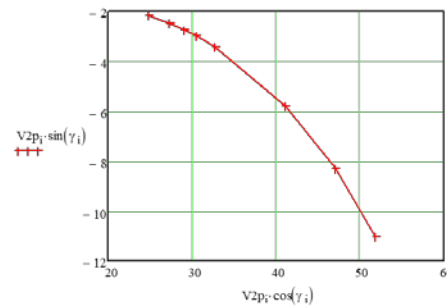


FIG. 24 The gliding characteristic

8. ELECTRO-ENERGETIC SYSTEM

According to the ISO 1540: 2006-Electric Power System [6], the Power System is the set of power sources and converters, their control and protection equipment, as well as electrical consumers connected through the distribution network. Figure 25 shows the power system of the UAV. From this it can be noticed that the electric energy is obtained with the generator and the on-board battery. This is used to provide UAV propulsion in VTOL mode, to power the equipment required for control and navigation as well as payload.

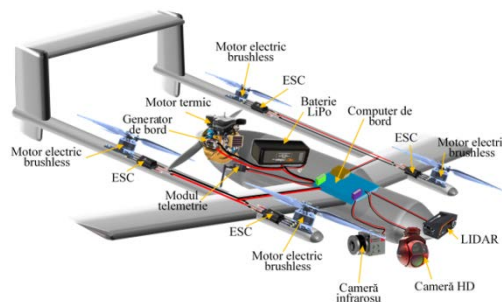


FIG. 25 The power system of the uav - biplane-quad-copter hybrid

9. ANALYSIS OF VTOL FLIGHT

To determine the engine power needed during VTOL flight, it is necessary to determine the traction force of the fixed wing vector in the takeoff and landing phase for different scenarios. Studying the type of missions of this type of UAV, 3 flight ceilings were established: 100m, 1000m and 2500m. Entering the specific data in the eCalc program [13] for the three flight ceilings we obtain:

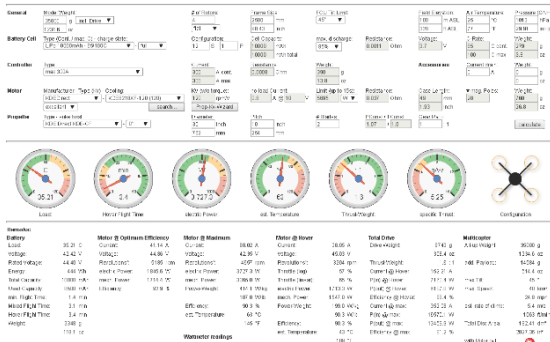


FIG. 26 The simulation data at 100m



FIG. 27 The simulation data at 1000 m



FIG. 28 The simulation data at 2500 m

Corroborating the results of the three scenarios, the following maximum engine power and hover power dependence on the altitude (Fig. 29) results:

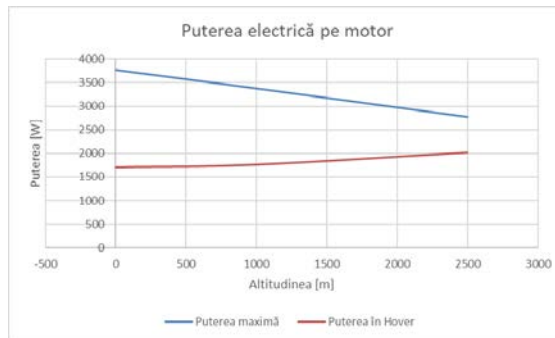


FIG. 29 Maximum and hover power

For designing the battery required to power the four KDE8218XF-120 motors, as well as the internal systems we propose the following scenarios:

1. The battery is used to secure the lifting of the fixed wing to ceiling 2500 m, 1000 m and 100 m, respectively, powering only the four KDE8218XF-120 motors without powering the onboard electronics;
2. Hover to the ceiling 2 min. required for the transition to and from the horizontal flight, and power the onboard electronics during the flight until the generator starts;
3. The battery is used both to ensure that the fixed wing vector is lifted to the flight ceiling, 2 min to hover for transition and to power the onboard electronics (if the generator failure is signaled).

From Flight Simulations we extract the following data:

Altitude [m]	Rate of climb [m/s]	Rate of descent [m/s]
100	5.4	3
1000	4.5	3
2500	1.3	3

with which the following durations are calculated:

Ceiling [m]	Climb time [s]	Descent time [s]
2500	670	833
1000	202	333
100	19	33

where an average descent speed of 3 m/s was assumed, regardless of altitude.

From the maximum power and hover:

Altitude [m]	Max Power [W]	Hover Power [W]
0	16762	7138
100	16570	7163
1000	14840	7391
2500	11985	8524

calculate an average power up to the flight ceiling, with which, for a battery 12S ($U = 44,4V$), the energy requirement is calculated for the three scenarios:

Altitude [m]	Battery capacity [Ah]			Flight time [min.]		
	Scenario 1	Scenario 2	Scenario 3	Scenario 1	Scenario 2	Scenario 3
100	63	70	96	11	13	27
1000	20	26	37	3.4	5.4	10.9
2500	2	7.4	8.6	0.3	2.3	2.9

The following characteristics are obtained:

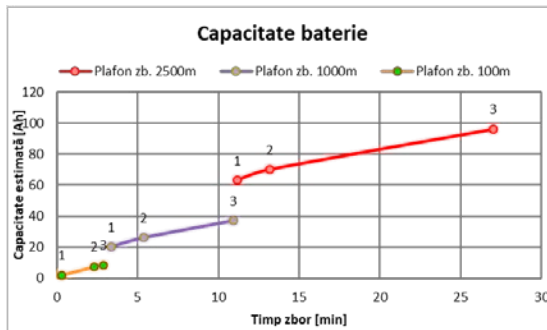


FIG. 30 Battery capacity

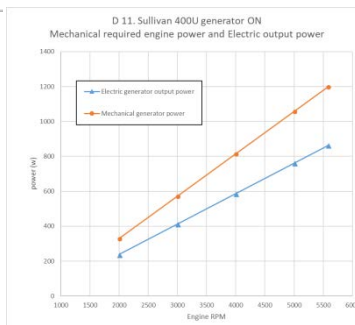


FIG. 31 Generated and required generator power

The following conclusions can be drawn:

- For Scenario 3 that requires the most battery, a capacity of about 100Ah is required, which requires a too heavy battery;
- For a capacity of 30Ah, the ceiling of approximately 1500m in Scenario 1, 1200m in Scenario 2, and 800m in Scenario 3 (generator failure and landing of the aircraft) can be reached.

- For a 30Ah capacity, the combined flight time would be about 8 minutes.

In conclusion we choose a 30Ah 12S3P battery with an approximate weight of 4kg.

For the onboard generator from the electrical characteristics of the generator it follows that the electric generated power at 4000rpm is 587W.

As the battery is 12S3P, with a voltage at 44.4 V, the voltage at the generator terminals, for the battery to charge, can be 50V, meaning a nominal current of 10A.

The time required to charge the battery in the most favorable condition (reaching the highest flight ceiling), Scenario 1, at approximately 1500 m is:

$$t_{\text{incărcare},1} = \frac{C}{I_N} = \frac{33 Ah}{10 A} = 3,3 h \quad (45)$$

But as the engine power during vertical descent is 1/3 of the maximum climb power, it turns out that only 1/3 of the battery capacity is required for safe landing, which means:

$$t_{\text{incărcare},2} = \frac{C/3}{I_N} = \frac{33 Ah/3}{10 A} = 1,1 h \quad (46)$$

an acceptable time for most flight missions.

10. CONCLUSIONS

A hybrid propulsion system for a fixed wing VTOL UAV was designed and tested. Shaft Power of the main engine was determined for a whole range of operating conditions were computed using an in-house developed mathematical model.

Propeller characteristics were determined and an original method to determine available power was used. With this, cruise, climb and descent performances of the aircraft were determined with in-house methodology and compared with result from commercial available software, result showing good agreement.

Takeoff and landing electric motors characteristics and hover time were determined from the power provided from the batteries. Also the time to recharge during cruise flight was assessed. Results shows good performances for the mission required.

REFERENCES

- [1] *** The UAVs. A brief introduction to the UAV Endurance. May 22, 2016. [Interactive] [Quoted: 30 October 2018] <http://www.theuav.com>;
- [2] Button, K., Powering Airlines with hydrogen, *Aerospace America*, Vol. 54, p. 5, 2016;
- [3] Daidzic, N. E., Piancastelli, L. și Cattini, A., Diesel engines for light-to-medium helicopters and airplanes, *International Journal of Aviation, Aeronautics, and Aerospace*, Vol. 1, 2014;
- [4] Frisch, A. M., Scaling Effects on the Performance and Efficiency of Gas Turbine Engines, Master of Science Project, University of California. Irvine, 2017;
- [5] Cirigliano, D., Engine-type and propulsion configuration selections for long-duration UAV flights, M.Sc. Thesis, Department of Aerospace Science and Technology, School of Industrial and Information Engineering, Politecnico di Milano, 2017;
- [6] ***. ISO 1540. 2006;
- [7] Patterson, D. J. și van Wylen, G., A digital computer simulation for spark-ignited engine cycles, in *Digital Calculations of Engine Cycles*, SAE Progress in Technology, Society of Automotive Engineers, Vol. 7, 1964;
- [8] M., M. Niță, F., V. Moraru și R., N. Patraulea, *Aeronave și rachete. concepte de proiectare*, Editura Militară, 1985;
- [9] A. Deperrois, et. al., XFLR5, [Interactive] [Quoted: 22 11 2018.], <http://www.xflr5.com/xflr5.html>;
- [10] Mark Drela, Harold Youngren, AVL, [Interactive] [Quoted: 22 11 2018], <http://web.mit.edu/drela/Public/web/avl/>;
- [11] Dr. Jan Roskam, DAR Corporation, *Advanced Aircraft Analysis*, [Interactive] [Quoted: 22 11 2018], <http://darcorp.com/Software/AAA/>;
- [12] Schenk, Helmut, Propeller Calculator, [Interactive] [Quoted: 22 11 2018], <http://www.drivecalc.de/PropCalc/>.
- [13] M., Muller, e-Calc the most reliable RC Calculator on the Web, [Interactiv] [Quoted: 22 01 2019] <https://www.ecalc.ch/>.